ACSNANO
www.acsnano.org
ARTICLE

Ultrasmall Magnetic $CuFeSe_2$ Ternary Nanocrystals for Multimodal Imaging Guided Photothermal Therapy of Cancer

Xinxin Jiang,[†] Shaohua Zhang,[†,‡] Feng Ren,[†] Lei Chen,[†] Jianfeng Zeng,[†] Mo Zhu,[§] Zhenxiang Cheng,[‡] Mingyuan Gao,[†] and Zhen Li*[,†]

[†]Center for Molecular Imaging and Nuclear Medicine, School for Radiological and Interdisciplinary Sciences (RAD-X), Soochow University, Collaborative Innovation Center of Radiation Medicine of Jiangsu Higher Education Institutions, Suzhou 215123, China

[‡]Institute for Superconducting and Electronic Materials Australian Institute for Innovative Materials, University of Wollongong, Wollongong, NSW 2500, Australia

[§]The First Affiliated Hospital of Soochow University, Shizi Jie 188, Suzhou 215006, China

Supporting Information

ABSTRACT: Nanoscale ternary chalcogenides have attracted intense research interest due to their wealth of tunable properties and diverse applications in energy and environmental and biomedical fields. In this article, ultrasmall magnetic $CuFeSe_2$ ternary nanocrystals (<5.0 nm) were fabricated in the presence of thiol-functionalized poly(methacrylic acid) by an environmentally friendly aqueous method under ambient conditions. The small band gap and the existence of intermediate bands lead to a broad NIR absorbance in the range of 500−1100 nm and high photothermal conversion efficiency (82%) of $CuFeSe_2$ nanocrystals. The resultant $CuFeSe_2$ nanocrystals show superparamagnetism and effective attenuation for X-rays. In addition, they also exhibit excellent water solubility, colloidal stability, biocompatibility, and multifunctional groups. These properties enable them to be an ideal nanotheranostic agent for multimodal imaging [*e.g.*, photoacoustic imaging (PAI), magnetic resonance imaging (MRI), computed tomography (CT) imaging] guided photothermal therapy of cancer.

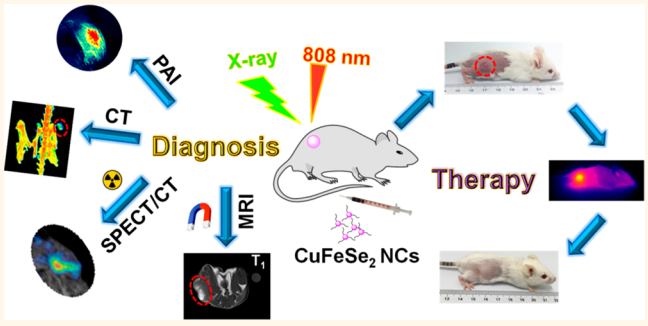

KEYWORDS: *multimodal imaging, photothermal therapy, ternary semiconductors, ultrasmall nanocrystals, magnetic $CuFeSe_2$*

During the past decade, near-infrared (NIR)-light-triggered photothermal therapy (PTT) of cancer has received great attention because of its minimal invasiveness, high spatial resolution, economic viability, and improved target selectivity.[1,2] Many photothermal transducers have been exploited for PTT of cancer, including metallic nanostructures (*e.g.*, Au, Ag, Pd), carbon-based nanomaterials (*e.g.*, carbon spheres, carbon nanotubes, graphene oxide), nanoscale metal chalcogenides (*e.g.*, $Cu_{2-x}E$, E = S, Se, and Te), transition metal dichalcogenide nanostructures (*e.g.*, WS_2, MoS_2, WSe_2), metal oxide nanoparticles (*e.g.*, WO_{3-x}, MoO_{3-x}), polymer nanoparticles (*e.g.*, polyaniline, polypyrrole), and organic dyes (*e.g.*, indocyanine green),[3−8] of which they either have a strong localized surface plasmon resonance (LSPR) absorbance in the NIR region, such as in the case of large metallic nanostructures and heavily self-doped semiconductors, or have a sufficiently narrow band gap. From the applications perspective, most currently available photothermal transducers have issues of either low conversion efficiency (η), lack of multifunctionality, or large particle size.

Because most photothermal transducers are employed for PTT and photoacoustic imaging (PAI), both which are based on the same photothermal conversion effect, the development of efficient transducers with high photothermal conversion efficiency (η) is highly significant. The η value has been improved from the initial ∼30% for Au and other metallic nanostructures[4] to ∼60% for copper chalcogenide nanostructures.[5,9,10] Recently, the photothermal conversion efficiency was further improved by engineering the composition and morphology of photothermal transducers. For example, an η of 73.4% was obtained in $CuCo_2S_4$ nanoparticles by the introduction of intermediate bands through cobalt ions into the

Received: February 14, 2017
Accepted: May 19, 2017
Published: May 19, 2017

DOI: 10.1021/acsnano.7b01032
ACS Nano 2017, 11, 5633−5645

fundamental gap of copper sulfide.[11] An η of 93.4% was achieved in porous Pd nanoparticles, which is higher than that of solid Pd nanocubes.[12]

The above examples clearly demonstrate the possibility of engineering photothermal transducers to achieve high conversion efficiency. In addition to high photothermal conversion efficiency, ideal photothermal transducers should exhibit complementary multifunctionality for achieving precise diagnosis and treatment. Most transducers are mainly used for PTT and/or PAI, in which PAI could overcome the disadvantages of conventional optical imaging with the advantages of deep penetration (up to 50 mm) and high sensitivity ($\sim 10^{-9}$ mol/L), but it has a low resolution (0.03−0.05 mm). Therefore, it is crucial to combine PAI with other complementary imaging modalities, such as magnetic resonance imaging (MRI) and single-photon emission computed tomography (SPECT), to realize high sensitivity and high resolution. In comparison, MRI has higher spatial resolution (10−100 μm), and SPECT has higher sensitivity (10^{-10}−10^{-12} mol/L).[13]

Compared with mono- and binary photothermal transducers, nanoscale ternary chalcogenides offer a broad spectrum for tuning their intrinsic optical, electronic, and magnetic properties for multimodal imaging and multiple therapies. One class of such chalcogenides is the magnetic ternary metal chalcogenides, in which magnetic ions not only induce interesting magnetic properties but also change their photoelectronic properties by the formation of intermediate bands in the fundamental gap. These properties have been exploited for diagnosis and treatment of cancer. For example, 10 nm $CuCo_2S_4$ nanocrystals prepared by a hydrothermal method were proven to be an efficient photothermal transducer (η = 73.4%) for photothermal therapy and a good contrast agent for MRI of tumors.[11] The 10 nm $CuFeS_2$ nanocrystals prepared by a hot-injection approach were also employed as an efficient photothermal transducer for *in vitro* photothermal ablation of tumor cells.[14] The 20 nm Cu_5FeS_4 nanocrystals obtained from the similar method were also employed as a photothermal transducer for photothermal therapy and as a contrast agent for MRI.[15] These examples clearly illustrate the potential of magnetic ternary nanocrystals in multimodal imaging and photothermal therapy, due to their impressive photothermal conversion efficiency and multifunctionality.

It should be noted that most works on magnetic ternary chalcogenide nanostructures are focused on Cu−Fe−S and Cu−Co−S nanocrystals, whereas less attention has been paid to Cu−Fe−Se nanostructures (*e.g.*, $CuFeSe_2$) due to the difficulties in the preparation of well-defined monodisperse and pure phase products. The smaller band gap of $CuFeSe_2$ (E_g = 0.16 eV) suggests higher photothermal conversion efficiency and better performance in PAI and PTT, in comparison with those ternary nanocrystals with wider band gaps.[16−19] However, the currently available $CuFeSe_2$ nanostructures are prepared by the hot-solution injection method,[20] the solventothermal process,[21] a high-temperature chemical method,[18] and other processes under harsh conditions. They have a large size and issues of water solubility and biocompatibility for bioapplications.

The ideal photothermal transducers should be also as small as possible to reduce their risk of rapid clearance by phagocytes and the reticuloendothelial system (RES). The small size could also endow them with quick clearance properties to reduce the potential side effects. It is well-known that nanoparticles can be cleared through two different routes after systemic administration, that is, through the liver (into bile) and through the kidneys (into urine).[22] The renal clearance route is favorable for inorganic nanostructures containing heavy and toxic metal ions because of the rapidity of this process. Whether nanoparticles can pass through the kidney is strongly dependent on their size, surface charge, and shape. To escape from the vascular compartment, nanoparticles have to pass through the endothelium with fenestrae (70−90 nm), the glomerular basement membrane (meshwork structure with 2−8 nm pores), and the epithelium with filtration slits (4−11 nm) between the podocyte extensions, three layers of glomerular capillary wall.[23] Due to the combined effects of each layer, it is easy for nanoparticles with a hydrodynamic diameter smaller than 6 nm to pass through the glomerular capillary wall, but it is difficult for larger nanoparticles. In this context, preparation of ultrasmall multifunctional photothermal transducers is highly significant. Most photothermal transducers, however, have an average size large than 5 nm.

In this article, ultrasmall magnetic $CuFeSe_2$ ternary nanocrystals (<5.0 nm) with high photothermal conversion efficiency (82%) were prepared by an environmentally friendly aqueous method under ambient conditions and labeled with radioactive ^{99m}Tc. These ternary photothermal transducers were successfully used for multimodal imaging [*i.e.*, MRI, PAI, SPECT, and computed tomography (CT) guided photothermal therapy of cancer.

RESULTS AND DISCUSSION

Ultrasmall magnetic $CuFeSe_2$ nanocrystals (NCs) were prepared by a wet chemistry method in aqueous solution under ambient conditions. As illustrated in Scheme 1, selenium

Scheme 1. Schematic Illustration of the Synthesis of Multifunctional $CuFeSe_2$ NCs

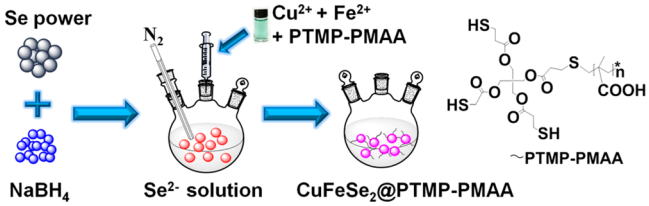

powder was first reduced by $NaBH_4$ in aqueous solution with magnetic stirring under inert atmosphere.[24,25] Then, a mixture of $CuCl_2{\cdot}2H_2O$, $FeSO_4{\cdot}2H_2O$, and trithiol-terminated poly(methacrylic acid) (PTMP−PMAA)[26,27] was immediately injected into the selenium precursor solution to form $CuFeSe_2$ NCs. The resultant nanoparticles were characterized with transmission electron microscopy (TEM) to determine their morphology and size. Small spherical particles with a size of 4.1 ± 0.4 nm are clearly observed (Figure 1a and Figure S1). The crystal structure of nanoparticles was revealed by their high-resolution TEM (HRTEM) image (Figure 1b), which clearly shows the lattice fringes with an interplanar spacing of 0.32 nm, matching well with (112) planes of tetragonal $CuFeSe_2$. The continuous selected area electron diffraction (SAED) rings in the inset further prove that the interplanar spacings are consistent with those of the (112) and (220) planes of the tetragonal structure. The crystal structures of $CuFeSe_2$ nanocrystals with or without PTMP−PMAA (P−P) were further characterized by X-ray powder diffraction (XRD), and the obtained patterns entirely fit well with that of tetragonal

DOI: 10.1021/acsnano.7b01032
ACS Nano 2017, 11, 5633−5645

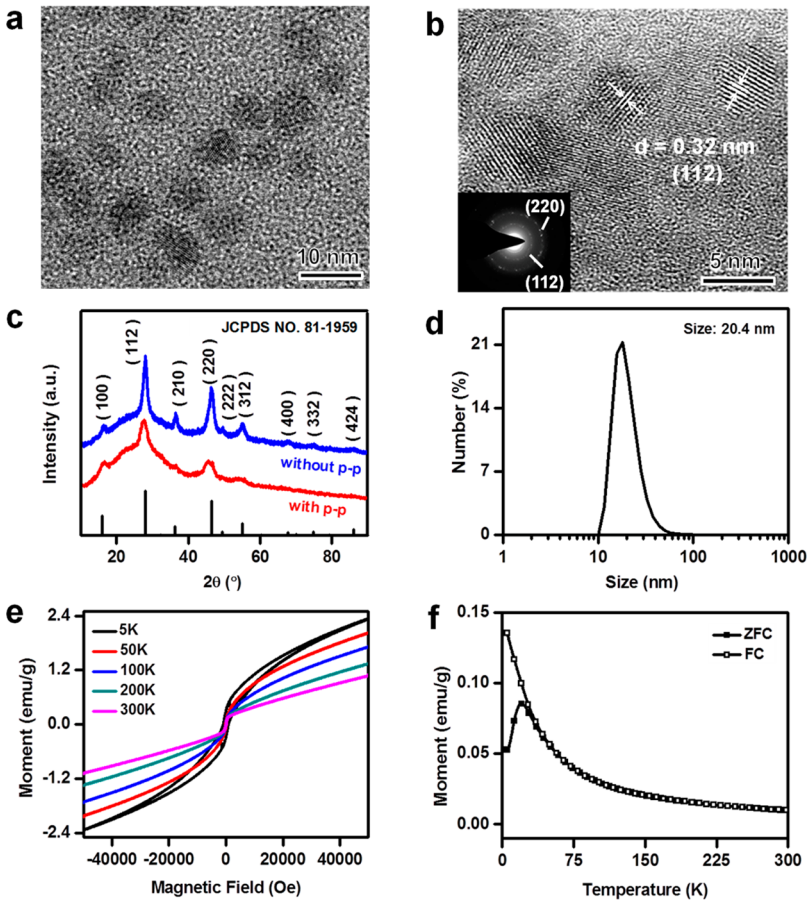

Figure 1. Characterization of as-prepared $CuFeSe_2$ NCs: (a) TEM image, (b) HRTEM image with corresponding SAED pattern (inset), (c) XRD patterns of $CuFeSe_2$ prepared with and without PTMP−PMAA (P−P) in comparison with the standard peaks of cubic berzelianite (JCPDS card no. 81-1959), (d) hydrodynamic size, (e) magnetization isotherms of $CuFeSe_2$ NCs at different temperatures, and (f) temperature dependence of the magnetization of $CuFeSe_2$ NCs measured in a field of 100 Oe.

eskebornite ($CuFeSe_2$, JCPDS no. 81-1959) (Figure 1c). The chemical composition of obtained nanocrystals was determined by electron energy loss spectroscopy (EELS) on the single-particle level (Figure S1c), which clearly reveals the coexistence of Cu, Fe, and Se elements in individual particles. The average atomic ratio of Cu/Fe/Se was determined to be 1.00:1.07:1.97 by inductively coupled plasma optical emission spectrometry (ICP-OES, Table S1). The binding energies of Cu 2p, Fe 2p, and Se 3d of resultant $CuFeSe_2$ NCs were determined by X-ray photoelectron spectroscopy (XPS) to reveal their valence states, which are +1, +3, and −2, respectively (Figure S2).

The above characterization results illustrate that pure $CuFeSe_2$ NCs can be simply synthesized from $CuCl_2$, $FeSO_4$, and Se precursors in aqueous solution under ambient conditions. The formation of $CuFeSe_2$ NCs involves the following key reactions. First, selenium powder was reduced by $NaBH_4$ in aqueous solution to form NaHSe (eq 1), which reacted with the mixture of $CuCl_2$ and $FeSO_4$ to generate FeSe and CuSe precipitates (eqs 2 and 3). Then the formed FeSe and CuSe precipitates further reacted and resulted in $CuFeSe_2$ nanocrystals (eq 4). To confirm eq 4, pristine FeSe and CuSe precipitates were prepared separately and then mixed in water and stirred for 40 min at room temperature. The suspension was centrifuged to collect precipitates, which were characterized by XRD (Figure S3a) to be $CuFeSe_2$ and unreacted precursors. The formation of $CuFeSe_2$ illustrates the spontaneous reaction between FeSe and CuSe.

$$2Se + 4NaBH_4 + 7H_2O \rightarrow 2NaHSe + Na_2B_4O_7 + 14H_2\uparrow \quad (1)$$

$$Fe^{2+} + HSe^- \rightarrow FeSe + H^+ \quad (2)$$

$$Cu^{2+} + HSe^- \rightarrow CuSe + H^+ \quad (3)$$

$$FeSe + CuSe \rightarrow CuFeSe_2 \quad (4)$$

It should be noted that $CuFeSe_2$ NCs can be also prepared from cuprous (Cu^+) and ferric (Fe^{3+}) precursors, and the crystal structures of the resultant nanocrystals were identified to be $CuFeSe_2$ by XRD (Figure S3b). The fundamental aspect for the formation of $CuFeSe_2$ NCs is that cuprous (Cu^+) and ferric (Fe^{3+}) ions are quickly transformed into cupric (Cu^{2+}) and ferrous (Fe^{2+}) ions through redox reactions when they are mixed together, which is confirmed by the similar absorption curves (Figure S3c) of the complexes formed between their mixtures with phenanthroline. The amount of Fe^{2+} formed from the cuprous (Cu^+) and ferric (Fe^{3+}) mixture is similar to that of a Cu^{2+} and Fe^{2+} mixture, as determined by their ultraviolet−visible (UV−vis) absorption spectra.

To characterize the surfaces of $CuFeSe_2$ NCs coated with polymer ligand, the Fourier transform infrared (FTIR) spectrum of as-prepared $CuFeSe_2$@PTMP−PMAA NCs (blue line in Figure S4a) was compared with that of PTMP−PMAA (red line in Figure S4a), in which both exhibit the characteristic

DOI: 10.1021/acsnano.7b01032
ACS Nano 2017, 11, 5633−5645

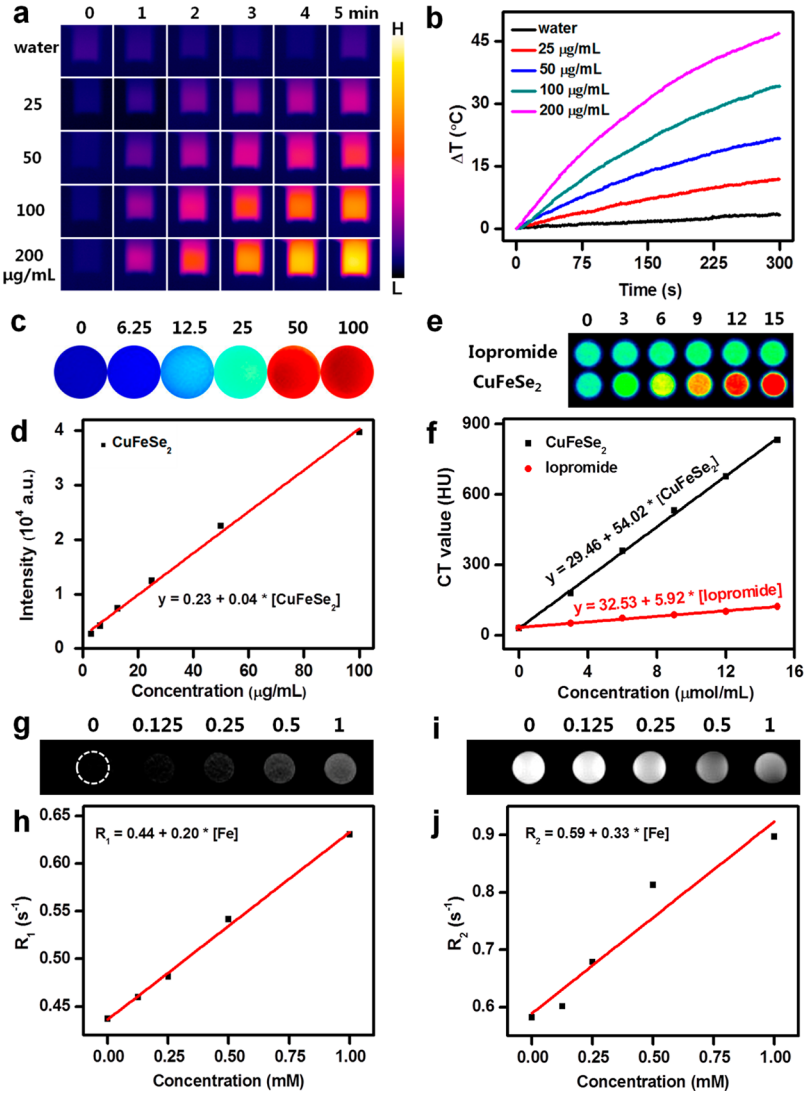

Figure 2. (a) Photothermal images and (b) corresponding heating curves of pure water and aqueous dispersions of $CuFeSe_2$ NCs at different concentrations under continuous irradiation by a 808 nm laser with a power density of 0.75 W/cm^2 for 5 min, (c) photoacoustic and (d) corresponding intensity of a series of $CuFeSe_2$ NC solutions with different concentrations, *i.e.*, 0, 6.25, 12.5, 25, 50, and 100 μg/mL from left to right. (e) CT images and (f) X-ray attenuation of intensity in Hounsfield units (HU) of $CuFeSe_2$ NCs as a function of $CuFeSe_2$ concentration in contrast to iopromide, (g–j) *in vitro* T_1- and T_2-weighted magnetic resonance imaging using different concentrations of $CuFeSe_2$ NCs. The longitudinal (r_1) and transverse (r_2) relaxivities of $CuFeSe_2$ NCs were determined to be 0.20 and 0.33 mM^{-1} s^{-1}, respectively.

peak of a carbonyl group at 1693 cm^{-1} (−CO−). Compared with PTMP−PMAA, the symmetric and asymmetric stretching bands of carboxylate (−COO−) in $CuFeSe_2$@PTMP−PMAA are, respectively, red-shifted from 1388 and 1482 cm^{-1} to 1411 and 1586 cm^{-1}. The difference between the symmetric and asymmetric bands is 96 cm^{-1} for PTMP−PMAA and 175 cm^{-1} for $CuFeSe_2$@PTMP−PMAA. The large difference indicates that the carboxylic groups of PTMP−PMAA had become coordinated with the surface metallic atoms of $CuFeSe_2$ NCs through a unidentate mode.[28] The polymer contents on the surfaces of $CuFeSe_2$ NCs were determined by thermogravimetric analysis (TGA) to be approximately 34.1 wt % (Figure S4b).

Both FTIR and TGA results demonstrate the successful coating of $CuFeSe_2$ NCs with PTMP−PMAA. The surface PTMP−PMAA endows them with excellent water solubility. Their hydrodynamic size was analyzed by dynamic light scattering (DLS) to be 20.4 nm (Figure 1d). Figure S5 shows photographs and UV−vis−NIR absorbance of $CuFeSe_2$ NC solutions with different concentrations. The broad absorbance in the NIR region (500−1100 nm) is attributed to the narrow band gap of $CuFeSe_2$, which arose from the formation of intermediate bands in the fundamental gap by Fe^{3+} ions.[11,14] The absorbance of $CuFeSe_2$ NCs at 808 nm is linearly increased with their concentration (Figure S5c). According to the Lambert−Beer law, their extinction coefficient is calculated to be 5.8 Lg^{-1}cm^{-1}, which is two times that of $Cu_{2-x}Se$ NCs (2.9 Lg^{-1}cm^{-1})[10] and higher than those of graphene oxide nanosheets (3.6 Lg^{-1}cm^{-1}) and Au nanorods (3.9 Lg^{-1}cm^{-1}) at this wavelength (*i.e.*, 808 nm).[29]

Due to their surface hydrophilic carboxylic groups and negative charges (ζ-potential of −34 mV), $CuFeSe_2$ NCs possess excellent solubility and stability in different media, such as H_2O, phosphate-buffered saline (PBS), 10% fetal bovine serum (FBS) solution, and low ionic strength saline (NaCl) solutions (*e.g.*, 0.5% NaCl, 1% NaCl, and 2.5% NaCl), as

DOI: 10.1021/acsnano.7b01032
ACS Nano 2017, 11, 5633−5645

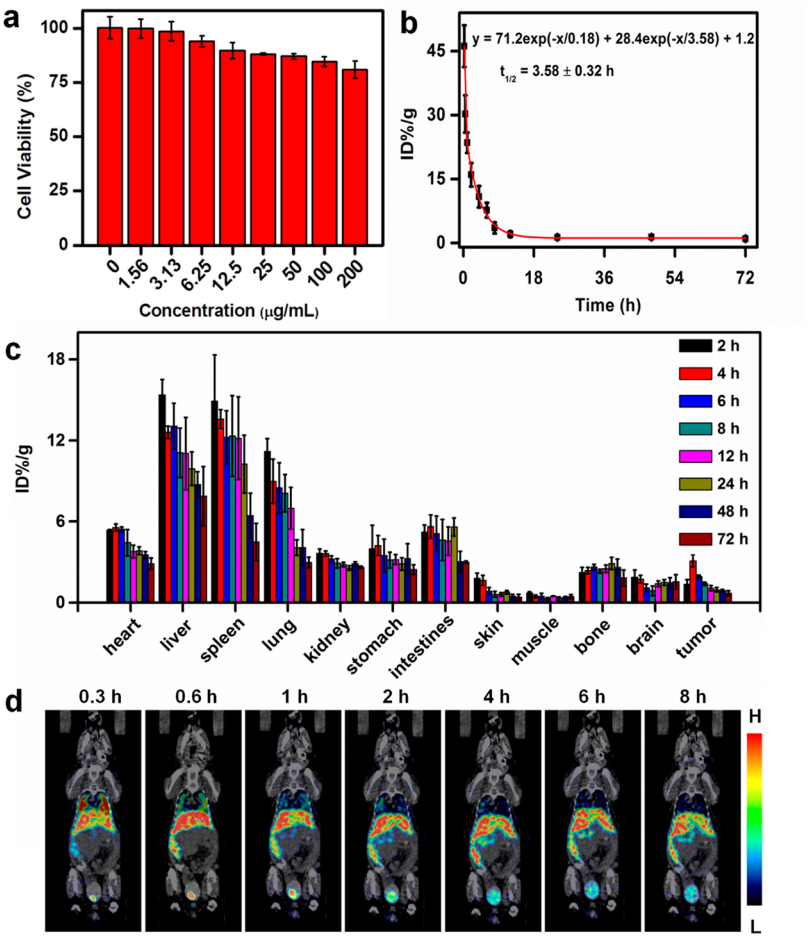

Figure 3. (a) *In vitro* relative cell viabilities of 4T1 cells after incubation with various concentrations of $CuFeSe_2$ NCs for 24 h; (b) blood circulation and (c) time-dependent biodistribution kinetics of $CuFeSe_2$ NCs after intravenous injection into mice, as determined by measuring Cu concentrations in organs, tissues, and blood samples with ICP mass spectrometry (ICP-MS); (d) *in vivo* SPECT/CT images of a mouse taken at different times after intravenous injection of $CuFeSe_2$–^{99m}Tc NC solution.

demonstrated by their similar absorbance and similar hydrodynamic size measured after they were dissolved in these media (Figure S6a–g). They are slightly aggregated over the time in highly concentrated NaCl solution (5%), which is indicated by the increase in the hydrodynamic size from 21 to 33 nm, as shown in Figure S6h. Their excellent colloidal stability is further demonstrated by the absence of precipitates or aggregates in their aqueous solutions during one month of storage (Figure S6i).

The introduction of magnetic Fe^{3+} ions induces very interesting magnetic properties. Figure 1e shows the magnetization isotherms (*i.e.*, *M*–*H* curves) of $CuFeSe_2$ NCs at different temperatures. Superparamagnetic characteristics with a magnetization value of 1.08 emu/g at 300 K were observed. As the temperature decreased from 300 to 5 K, $CuFeSe_2$ NCs experienced a transition from paramagnetism to ferromagnetism. To determine their transition temperature, zero-field cooling (ZFC) and field cooling (FC) measurements were carried out between 5 and 300 K in an applied magnetic field of 100 Oe (Figure 1f). The ZFC and FC curves diverged around 70 K, which is the transition temperature and consistent with previous reports.[30−32] The magnetic results suggest the potential of $CuFeSe_2$ NCs as a contrast agent for MRI.

The broad NIR absorbance and the large extinction coefficient of $CuFeSe_2$ NCs guarantee their excellence in photothermal conversion. The particle solutions with different concentrations were irradiated continuously with an 808 nm laser (0.75 W/cm^2) for 300 s, and their temperatures were recorded with an infrared thermal imaging camera. Figure 2a,b clearly demonstrates the strong dependence of the photothermal conversion of $CuFeSe_2$@PTMP–PMAA NCs on their concentration, and the temperature increments (ΔT) can be finely tuned between 3 and 47 °C by simply changing their concentrations. The photothermal conversion efficiency is calculated to be 82%, and the detailed calculations are shown in the Supporting Information (Figure S7a,b). The high conversion efficiency is attributed to the narrow band gap and intermediate bands formed by introduction of Fe^{3+} ions. In addition to high conversion efficiency, $CuFeSe_2$ NCs also exhibit excellent photothermal stability (Figure S7c), which is an important feature for photothermal transducers.

The above remarkable photothermal conversion performance suggests that $CuFeSe_2$ NCs could be a promising photothermal transducer for PA imaging. The *in vitro* PA imaging was performed with a laser wavelength of 680 nm. The photoacoustic signal was significantly enhanced with the assistance of $CuFeSe_2$ NCs, and it was linearly increased with increasing concentration (Figure 2c,d), which highlights the potential of $CuFeSe_2$ NCs for PA imaging.

DOI: 10.1021/acsnano.7b01032
ACS Nano 2017, 11, 5633–5645

The heavy Fe, Cu, and Se elements suggests the potential of $CuFeSe_2$ NCs in X-ray imaging. The attenuation of X-rays in ternary $CuFeSe_2$ could be considered as the sum of attenuations in the individual elements, and the total attenuation coefficient (μ) can be expressed by eq 5:

$$\mu_{CuFeSe_2} = 0.23\mu_{Cu} + 0.20\mu_{Fe} + 0.57\mu_{Se} \quad (5)$$

where μ_{Cu}, μ_{Fe}, and μ_{Se} are the attenuation coefficients of Cu, Fe, and Se, respectively. There are three interactions between X-rays and individual elements, such as coherent scattering (ω), the photoelectric effect (τ), and Compton scattering (σ). Therefore, each attenuation coefficient (μ) can be expressed by eq 6:[33]

$$\mu = \omega + \tau + \sigma \quad (6)$$

The minor contribution of coherent scattering could be excluded without consideration. Due to the fact that the photoelectric effect is from the interactions between the X-ray photons and the inner shell electrons, the atomic number (Z) and photon energy (E) significantly influence this process through eqs 7 and 8:

$$\tau \propto Z^3 \quad (7)$$

$$\mu \propto \frac{1}{E^3} \quad (8)$$

which clearly show that an element with high Z has a pronounced photoelectric effect, whereas the high photon energy means less contribution to μ. In contrast, Compton scattering occurs when X-ray photons collide with outer-shell electrons, and it gradually diminishes with the increasing X-ray photon energy. Therefore, the contribution of Compton scattering is high for an element with low Z, but it is very low for one with high Z.

$$\bar{Z} = \sqrt[2.94]{Z_{Cu}^{2.94} + Z_{Fe}^{2.94} + 2Z_{Se}^{2.94}} \quad (9)$$

In our case, the effective atomic number of $CuFeSe_2$ is calculated to be 49.85 through eq 9, and the X-ray attenuation coefficient (μ) is calculated to be 1.94 cm^2/g for 60 keV X-rays by eq 5.[34,35] Both μ and $\bar{Z}$ are larger than that of $Cu_{2-x}Se$ due to the introduction of Fe^{3+} ions, which demonstrates the potential of $CuFeSe_2$ NCs in CT imaging.[10,36] Figure 2e,f displays the CT images and Hounsfield unit (HU) values of different concentrations of $CuFeSe_2$ NCs in comparison with the clinically used iopromide. A well-correlated linear relationship is observed, and the slope of the HU value against the concentration is approximately 54.0 HU L/mmol, which is nine times that of commercial iopromide (5.9 HU L/mmol), due to the larger attenuation coefficient and the similar effective atomic number to iodine (Z = 53).

In addition to PA imaging and CT imaging, the *in vitro* MRI imaging performance of as-prepared $CuFeSe_2$ NCs was evaluated with a clinically used 3.0 T MRI instrument. Figure 2g–j shows typical T_1- and T_2-weighted images of $CuFeSe_2$ NCs. Their longitudinal and transverse relaxivities (r_1, r_2) are, respectively, calculated to be 0.2 and 0.33 mM^{-1} s^{-1}, which are comparable to those of weak magnetic nanoparticles; for example, r_1 and r_2 of MnO nanoparticles are 0.12 and 0.44 mM^{-1} s^{-1}, respectively.[37]

The *in vitro* imaging results indicate the robustness of $CuFeSe_2$ NCs as a contrast agent for *in vivo* multimodal imaging if they are safe and have good biocompatibility. Therefore, the potential cytotoxicity of the $CuFeSe_2$ NCs was assessed through a standard MTT [(3-(4,5-dimethylthiazol-2-yl)-2,5-diphenyltetrazolium bromide)] assay with 4T1 cells (murine breast cancer cells). The results in Figure 3a demonstrate that $CuFeSe_2$ NCs have good biocompatibility, and no serious cytotoxicity toward 4T1 cells was observed in the range of 0–200 μg/mL, in which the cell viability was higher than 80%. Then, the circulation behavior of $CuFeSe_2$ NCs in the blood was assessed by determining the Cu contents in blood samples withdrawn at different intervals after intravenous injection of the nanocrystals into healthy mice. Due to their small size, $CuFeSe_2$ NCs exhibit a blood circulation time of around 3.6 h, as shown in Figure 3b.

The accumulation and metabolism of $CuFeSe_2$ NCs were investigated after they were intravenously injected into 4T1 tumor-bearing BALB/c mice (200 μL, 2 mg/mL). The time-dependent biodistributions of nanoparticles (characterized with Cu contents) in the tumor and in the major organs are shown in Figure 3c. The accumulation of nanoparticles is in the order of liver ≈ spleen > lung > intestine > heart > stomach > kidney > bone > tumor > brain > skin > muscle. The Cu contents in the liver and spleen reached 16 ID%/g (percentage of injected dose per gram tissue) and 15 ID%/g at 2 h postinjection and then decreased to 8 and 5 ID%/g at 72 h, respectively. Their higher contents are attributed to the rich phagocytes in the liver and spleen, which can readily eliminate nanoparticles larger than 10 nm.[38] Similarly, the Cu contents in the lung gradually decreased from 11 ID%/g at 2 h postinjection to 3 ID%/g at 72 h postinjection. The fast decrease in the Cu contents in these organs indicates the easy degradation of ultrasmall nanoparticles.

There are around 4 ID%/g of nanoparticles excreted by the kidney. The less renal clearance of $CuFeSe_2$ nanoparticles is due to their average hydrodynamic size (D_h = 20.4 nm), which is larger than the threshold of the glomerular capillary wall, and their negatively charged surfaces (ζ-potential of −34 mV), both which make the complete renal clearance difficult. The nanoparticles found in urine were characterized to be $CuFeSe_2$ with TEM (Figure S8). The small $CuFeSe_2$ NCs can be also accumulated in the tumor through the enhanced permeability and retention (EPR) effect due to the leaky blood vasculature in tumors, and the maximum Cu contents in tumor were 3.2 ID %/g at 4 h postinjection.

To further demosntrate the dynamic distribution of nanoparticles, $CuFeSe_2$@PTMP–PMAA NCs were chelated with radioactive technetium-99m (^{99m}Tc, half-life, $t_{1/2}$ = 6.02 h, γ-ray energy, E_r = 140 keV) through their surface multifunctional groups (−COOH and − SH), with a labeling yield of 57%. The colloidal stability of labeled nanoparticles (denoted as $CuFeSe_2$–^{99m}Tc NCs) was assessed by determining their hydrodynamic size with the DLS method. As shown in Figure S9a,b, there is no big difference in their hydrodynamic size before and after labeling with ^{99m}Tc. ^{99m}Tc was tightly bound with $CuFeSe_2$ NCs, and the overall relative radioactivity in H_2O and 10% FBS was decreased slightly over time and maintained at around 80% (Figure S9c,d). The distribution of labeled nanoparticles in major organs was quantified by counting γ-rays from the SPECT/CT images, which were successively acquired at 0.3, 0.6, 1, 2, 4, 6, and 8 h after they were intravenously injected into 4T1 tumor-bearing mice (Figure 3d and Figure S10). A high uptake of $CuFeSe_2$ NCs in the liver, spleen, and bladder was observed (Figure S10f). The quantification of dynamic accumulation of $CuFeSe_2$–^{99m}Tc NCs in the tumor (Figure 4a) shows that the intensity of the γ-rays increased with

DOI: 10.1021/acsnano.7b01032
ACS Nano 2017, 11, 5633–5645

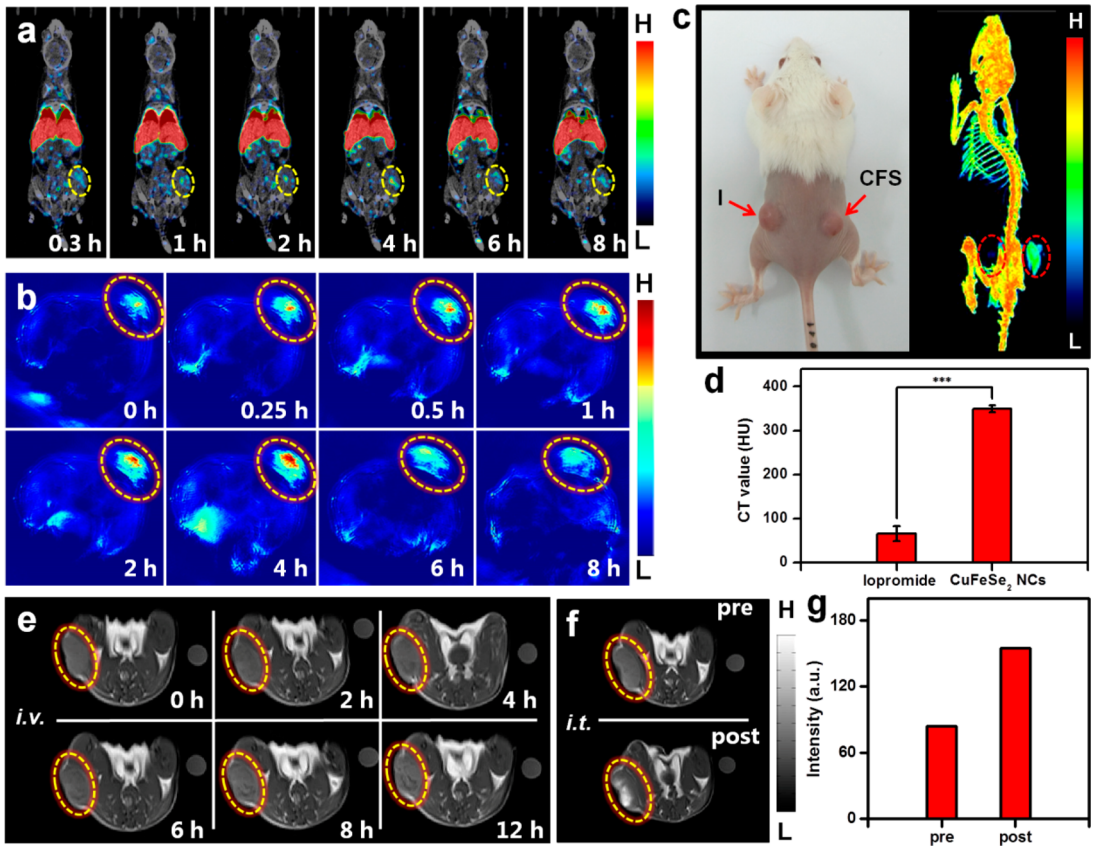

Figure 4. (a) SPECT images of a mouse bearing a tumor (indicated by the yellow circles) after intravenous injection of $CuFeSe_2$—^{99m}Tc NCs; (b) *in vivo* PA images of tumor (indicated by the yellow circles), acquired at 0, 0.25, 0.5, 1, 2, 4, 6, and 8 h after the mouse was intravenously injected with $CuFeSe_2$ NCs (dose = 6 mg/kg); (c) photograph and 3D *in vivo* CT image, and (d) signal intensity of a mouse bearing two tumors after intratumoral injection of iopromide (I, left) and $CuFeSe_2$ NCs (CFS, right) with the same concentration (dose = 25 mg/kg, $*p < 0.5$, $**p < 0.01$, $***p < 0.001$); (e) T_1-weighted MRI images of mice collected at 0, 2, 4, 6, 8, and 12 h after intravenous (i.v.) injection of $CuFeSe_2$ NCs (dose = 20 mg/kg); (f, g) T_1-weighted MRI images and signal intensity of mice collected pre- and post-intratumoral injection of $CuFeSe_2$ NCs.

time and reached its maximum of 1.93 ID%/g at 4 h postinjection (Figure S11a).

To demonstrate whether the accumulated $CuFeSe_2$ NCs through the EPR effect are enough for the *in vivo* multimodal imaging of tumors, 200 μL of $CuFeSe_2$ NCs (0.6 mg/mL) was intravenously injected into 4T1 tumor-bearing mice. First, PA imaging was performed at different intervals of postinjection (Figure 4b and Figure S11b). The tumor area was gradually enhanced to the brightest at around 4 h postinjection and then gradually reduced to the control level. The maximum tumor signal is about two times higher than control level. The time-dependent PAI signal demonstrates the dynamic accumulation of nanocrystals in the tumor, which is similar to the observations in other organs such as spleen and liver (Figure S12).

Second, the same amount of $CuFeSe_2$ NCs was intravenously injected into mice bearing 4T1 tumors, and CT images were acquired at different time points. No obvious enhancement was observed, however, because there was less passive accumulation of nanocrystals in the tumor (<5 ID%/g). Therefore, the potential of $CuFeSe_2$ NCs in CT imaging was demonstrated by intratumoral injection of nanocrystals, in comparison with commercial iopromide. Both contrast agents were injected into two tumors on the same mouse with the same dose (25 mg/kg). Figure 4c,d shows drastic enhancements after injection of the two agents, and $CuFeSe_2$ NCs exhibit better performance than iopromide, as indicated by the higher CT values (349.23 *vs* 65.69 HU). The results demonstrate the superior CT imaging performance of the $CuFeSe_2$ NCs as a contrast agent if they are accumulated sufficiently in the lesion area.

Third, 200 μL of $CuFeSe_2$ NCs (2 mg/mL) was intravenously administered into 4T1 tumor-bearing mice, which were imaged at 0, 2, 4, 6, 8, and 12 h with a clinically used 3.0 T MR instrument (Figure 4e). The results clearly show gradual enhancement of the tumor area with the accumulation of nanoparticles; that is, 12% positive enhancement was observed in T_1-weighted MRI images (Figure S11c). To further demonstrate the pronounced enhancement of MRI, a $CuFeSe_2$ NC solution (50 μL, 10 mg/mL) was intratumorally injected, and then MRI images of the tumor were acquired (Figure 4f,g). The drastic enhancement demonstrates that $CuFeSe_2$ NCs can significantly shorten the longitudinal relaxations of water protons if they are accumulated sufficiently in the tumor.

The above *in vitro* and *in vivo* imaging results demonstrate that $CuFeSe_2$ NCs are promising in multimodal imaging and in photothermal therapy of cancer, as illustrated in Scheme 2. A major concern for these *in vivo* theranostic applications of $CuFeSe_2$ NCs is their immune response, which was investigated by blood routine examination and blood biochemistry analysis (Figure 5). The inflammatory response induced by any side effects of a foreign substance could be reflected in hematological factors.[39] Four groups of healthy BALB/c mice

DOI: 10.1021/acsnano.7b01032
ACS Nano 2017, 11, 5633–5645

Scheme 2. Illustration of Multimodal Imaging (PAI, CT, SPECT/CT, MRI) and Photothermal Therapy of Cancer Using $CuFeSe_2$ NCs

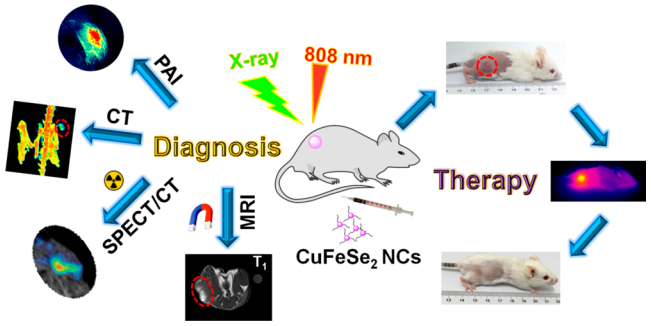

were intravenously injected with $CuFeSe_2$ NCs at a dose of 20 mg/kg. The mice were sacrificed at day 1, day 5, day 10, and day 15 to collect blood samples for analysis. The detected blood indices include hemoglobin (HGB), white blood cells (WBC), red blood cells (RBC), mean corpuscular volume (MCV), platelet (PLT), and hematocrit (HCT). There is no notable difference in HGB, MCV, or PLT between the treated and untreated mice. The slight decreases in the WBC and HCT in the mice on day 1 and day 5 after treatment and gradual recovery to the level of untreated mice at day 10 and day 15 indicate a mild immunological stress.

The slight decrease in total protein (TP) in serum biochemical analysis performed on day 1 and day 5 implies a potential inflammation caused by disorder in the immune system. As mentioned previously, nanoparticles can be cleared through the liver into bile and through the kidneys into urine. The level of alanine aminotransferase (ALT) reflects the liver function, and urea nitrogen (UREA) is a specific serological index for the kidney function. The slight decrease in UREA on day 1 and day 5 is consistent with the variation of RBC, HCT, TP, and ALB. The recovery of all detected indices obtained through the blood sample count on day 15 suggests that $CuFeSe_2$ NCs are less toxic.

The minor immune response and less toxicity suggest that $CuFeSe_2$ NCs could be used for *in vivo* photothermal therapy of cancer, as they can efficiently convert NIR light into heat with an efficiency of 82%. Prior to the *in vivo* experiments, the *in vitro* photoablation of cancer cells was performed using 4T1

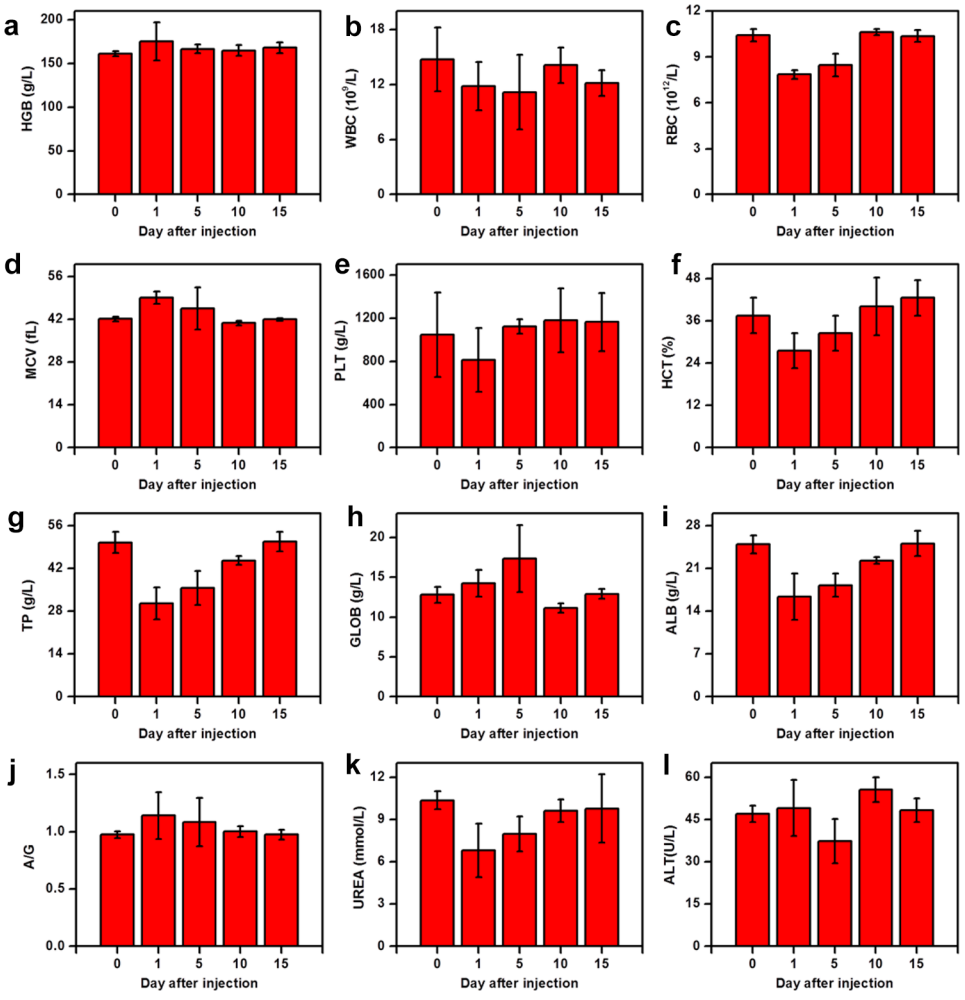

Figure 5. (a–l) Blood biochemistry of female BALB/c mice treated with $CuFeSe_2$ NC solution at a dose of 20 mg/kg. Four mice without injection were used as untreated control mice. Time course changes of hemoglobin (HGB, a), white blood cells (WBC, b), red blood cells (RBC, c), mean corpuscular volume (MCV, d), platelets (PLT, e), hematocrit (HCT, f), total protein (TP, g), globulin (GLOB, h), albumin (ALB, i), ratio of albumin to globulin (A/G, g), urea nitrogen (UREA, k), and alanine aminotransferase (ALT, l) from control mice (0) and $CuFeSe_2$ NC-treated mice. Statistics are based on four mice per data point.

DOI: 10.1021/acsnano.7b01032
ACS Nano 2017, 11, 5633–5645

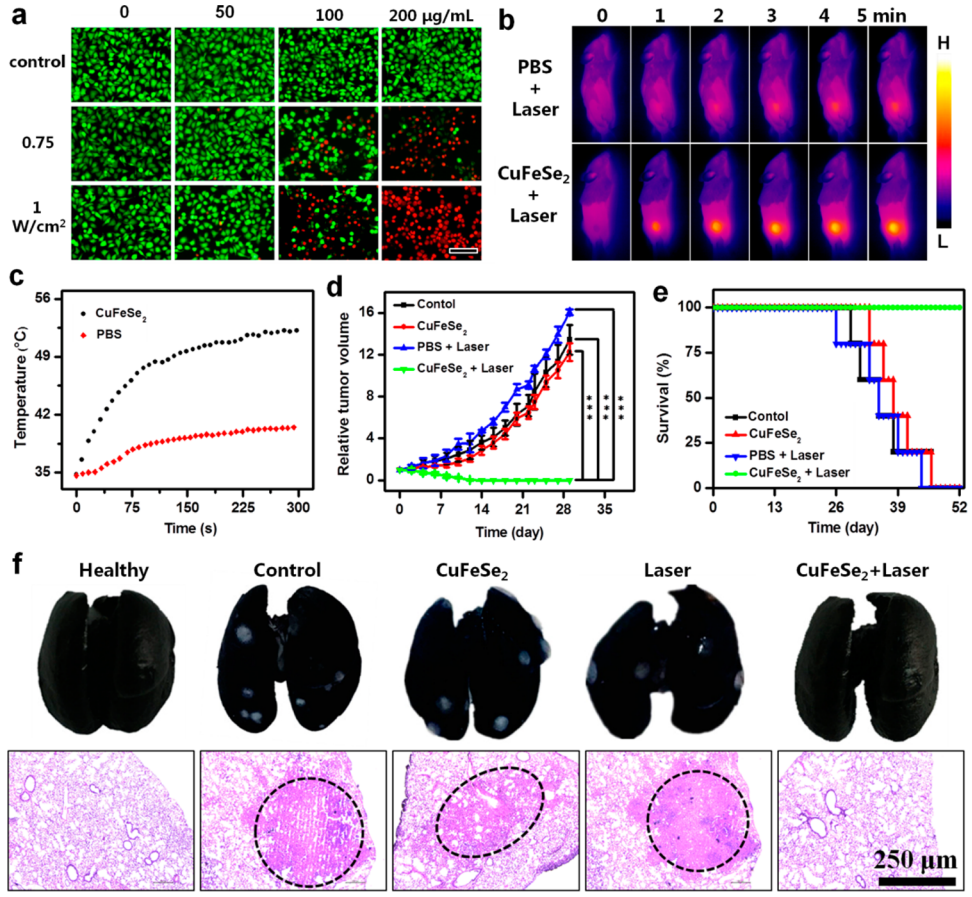

Figure 6. (a) Fluorescence images of 4T1 cells stained with live/dead kit after *in vitro* photothermal ablation under NIR laser irradiation with and without $CuFeSe_2$ NC solutions in different concentrations, with the scale bar = 100 μm. (b) Infrared thermal images and (c) temperature curves of 4T1 tumor-bearing mice intravenously injected with $CuFeSe_2$ NC solution (dose = 20 mg/kg) and then irradiated with an 808 nm NIR laser at a power density of 1 W/cm^2 for 5 min, in comparison with injection of PBS solution followed by NIR irradiation. (d) Relative tumor volumes normalized to their initial volumes (analysis of variance was used to assess statistical significance; $*p < 0.5$, $**p < 0.01$, $***p < 0.001$). (e) Survival curves of different groups of mice after various treatments. (f) Photographs of whole lungs stained with India ink and lung slices stained with hematoxylin and eosin (H&E) from different groups of mice, with the abnormal tissues caused by tumor metastasis highlighted by dashed circles.

cells, which were cultured with 0, 50, 100, and 200 μg/mL of $CuFeSe_2$ NCs and then exposed to an 808 nm laser with power densities of 0.75 and 1 W/cm^2 for 5 min. Figure S13a shows time-dependent temperature curves of the cells exposed to the laser with different power densities after incubation. A strong dependence of temperature on laser intensity was clearly observed. After photothermal ablation, the living and dead cells were stained and shown in Figure 6a, where the number of dead cells (red) increased with both the concentration of $CuFeSe_2$ NCs and the laser power density. These results illustrate the feasibility of killing cancer cells by using $CuFeSe_2$ NCs as a photothermal transducer.

Based on the above results, four groups of 4T1 tumor-bearing mice (7 mice per group) were used to demonstrate *in vivo* photothermal therapy of cancer under the guidance of multimodal imaging. The mice in the treatment group were intravenously administered $CuFeSe_2$ NCs (20 mg/kg) with a single dose and then irradiated with an 808 nm laser at a power density of 1 W/cm^2 for 5 min at 4 h postinjection. Three other control groups were denoted as (1) mice without any treatment (control group), (2) mice only injected with $CuFeSe_2$ NCs without laser irradiation ($CuFeSe_2$ group), and (3) mice injected with PBS and irradiated with the laser (PBS + laser group). Figure 6b,c compares the tumor temperatures of the mice injected with $CuFeSe_2$ NCs and the mice injected with PBS, both which were irradiated with the 808 nm laser under the same conditions. The tumor temperature of mice in the treatment group increased quickly and reached ~52 °C within 5 min, which is much higher than that of the mice administered with PBS (40 °C). The relative higher tumor temperature in the treatment group than in control groups could effectively kill cancer cells, which was demonstrated by the hematoxylin and eosin (H&E) staining of tumor slices from different groups of mice at day 1 (Figure S13b). There was severe damage to tumor cells of mice in the treatment group, but no obvious necrosis was found in three control groups.

Photographs of the mice (Figure S14), their body weights (Figure S15a), and the tumor volume (Figure 6d and Figure S15b) were taken and measured every 2 days after different treatments. The negligible difference in the body weights of the four groups of mice indicates that the current dose of $CuFeSe_2$ NCs did not induce acute toxicity or noticeable systemic toxicity. This is further supported by the absence of damage and inflammation in the major organs (*e.g.*, heart, liver, spleen, lung, and kidney) of mice from the treatment group that were harvested at day 1, day 7, and day 21 after H&E staining

DOI: 10.1021/acsnano.7b01032
ACS Nano 2017, 11, 5633−5645

(Figure S16). The staining results are consistent with those for healthy mice. The tumors of mice in the treatment group became smaller and smaller after PTT treatment and finally disappeared without relapse (Figure 6d and Figure S15b). As a consequence, all the mice lived well and survived (Figure 6e). In contrast, the tumors in other three groups kept growing with a similar trend, and they cannot be completely eradicated through laser irradiation or administration of $CuFeSe_2$ NCs alone. Moreover, the tumors grew faster after laser irradiation in comparison with the mice without any treatment and the mice only injected with $CuFeSe_2$ NCs, which suggests that appropriate heat could promote the proliferation of tumor cells (Figure 6d). All the mice from the three control groups died eventually (Figure 6e).

The above treatment shows excellent results for the photothermal therapy of cancers with the assistance of $CuFeSe_2$ NCs due to their high conversion efficiency. To further demonstrate the effectiveness of treatment without tumor metastasis, the lungs and livers of the mice in different groups were carefully examined because pulmonary and hepatic metastases are very common for breast cancer and usually lead to high mortality. As revealed by the photographs of lungs stained with India ink (Figure 6f), no obvious pulmonary metastasis was observed in the mice from the treatment group after 30 days post-treatment, in comparison to the healthy mice. Metastasis was not observed in the heart, spleen, or kidney of mice from the treatment group (Figure S17). In contrast, aggressive lung metastases were found in the mice from the other three groups after 30 days post-treatment. The H&E staining of lung and liver slices further demonstrates the effectiveness of photothermal therapy, by comparison with the healthy mice and the mice with metastasis in the other groups.

CONCLUSION

In summary, sub-5 nm ternary $CuFeSe_2$ NCs stabilized with PTMP−PMAA were successfully prepared by an environmentally friendly aqueous route under ambient conditions. The resultant ultrasmall $CuFeSe_2$ NCs exhibit broad NIR absorbance, high photothermal conversion efficiency, superparamagnetism, and effective attenuation of X-rays, in addition to possessing excellent colloidal stability, biocompatibility, and multifunctional groups. These excellent properties enable them to be a promising nanotheranostic agent for *in vivo* multimodal imaging (PA, MR, CT, SPECT/CT) and photothermal therapy of cancer. Their excellence in theranostics highlights the potential of the ultrasmall ternary chalcogenide nanocrystals in precise diagnosis and treatment of cancer.

EXPERIMENTAL SECTION

Materials. Copper(II) chloride dihydrate ($CuCl_2{\cdot}2H_2O$, ≥99%), ferrous (II) sulfate heptahydrate ($FeSO_4{\cdot}7H_2O$, ≥99%), selenium powder (Se, ≥99.5%), and sodium borohydride ($NaBH_4$, 99%) were bought from Sigma-Aldrich. Thiol-functionalized poly(methacrylic acid) with a number-average molecular weight of 6359 g/mol and a polydispersity of 1.18 was prepared as described elsewhere.[40−42] Milli-Q water with a resistivity above 18 MΩ·cm was used in the experiments.

Preparation of $CuFeSe_2$@PTMP−PMAA Nanocrystals. In a typical synthesis, 39.48 mg of Se powder was dispersed in 100 mL of Milli-Q water, and then 50 mg of $NaBH_4$ was added to reduce it at ambient conditions with protection of nitrogen flow. A 5 mL mixture of $CuCl_2{\cdot}2H_2O$ (42.62 mg), $FeSO_4{\cdot}7H_2O$ (69.75 mg), and PTMP−PMAA (400 mg) was separately prepared. After Se powder was completely reduced, the above mixture was added into the selenium precursor solution immediately to form a black solution. The resultant solution was ultrafiltrated through a membrane with a molecular weight cutoff (MWCO) of 100 kDa with a speed of 3500 rpm. The supernatant solution was dialyzed against Milli-Q water (MWCO of 8−14 kDa) subsequently for 48 h to remove impurities. The purified $CuFeSe_2$ NC solution was concentrated by a similar ultrafiltration method and stored at 4 °C for further characterization and application. CuSe and FeSe nanoparticles were prepared by the similar method except that different amounts of $NaBH_4$ and Se powder were used.

Characterization. The size and morphology of $CuFeSe_2$ NCs were characterized with a FEI Tecnai F20 transmission electron microscope operating at 200 kV. The crystallography structure of $CuFeSe_2$ NCs was determined by the powder XRD, which was recorded using a Shimadzu XRD-6000 diffractometer with a radiation wavelength of 0.15406 nm from Cu $K\alpha_1$. Their hydrodynamic size was determined by a Malvern Zetasizer Nano ZS90 armed with a solid-state He−Ne laser (λ = 633 nm) at 25 °C. The absorbance of $CuFeSe_2$ NC solution was measured with a PerkinElmer Lambda 750 UV−vis−NIR spectrophotometer. The valence states of elements in $CuFeSe_2$ NCs were determined by XPS measurements, which were recorded using a Thermo Scientific Sigma Probe instrument with Al $K\alpha$ X-ray radiation and fixed analyzer transmission mode. The coordination environment of $CuFeSe_2$ NCs with surface polymer ligands was characterized with a Nicolet iS50 FTIR spectrometer in a range of 400−3500 cm^{-1}. The polymer contents were determined by TGA, which was performed under nitrogen atmosphere with a heating rate of 10 °C/min from room temperature to 700 °C on a synchronous thermal analyzer (DSC/DTA-TG, STA 449 F3 Jupiter).

Photothermal Effect, Photostability, and Photothermal Conversion Efficiency. A series of $CuFeSe_2$ NC solutions with concentrations of 0, 25, 50, 100, and 200 μg/mL were irradiated with an 808 nm laser (Hi-Tech Optoelectronics Co., Ltd. Beijing, China), and their temperatures were recorded with an infrared thermal imaging camera (FLIR, A65). The photostability of $CuFeSe_2$ NCs was estimated by irradiating 50 μg/mL solution in a quartz cuvette with an 808 nm laser (0.75 W/cm^2) for 5 min (laser on) and then cooling to room temperature without irradiation (laser off). Such heating/cooling processes were repeated five times to test the photostability. To determine the photothermal conversion efficiency (η) of $CuFeSe_2$ NCs, 50 μg/mL solution was continuously irradiated with an 808 nm laser (0.75 W/cm^2) to reach a steady temperature, and then the laser was turned off to allow the solution to naturally cool to room temperature. The details of calculations are given in the Supporting Information.

Cytotoxicity of the $CuFeSe_2$@PTMP−PMAA NCs. The 4T1 cells (1×10^4 cells per well) were seeded into 96-well plates in the standard cell media, cultured at 37 °C in a 5% CO_2 atmosphere, and then incubated with $CuFeSe_2$ nanocrystals in different concentrations (1.56, 3.13, 6.25, 12.5, 25, 50, 100, and 200 μg/mL) for 24 h. The relative cell viabilities were determined by the standard MTT assay.

Blood Test and Bioanalysis. The blood samples were collected from four groups of mice (4 mice/group) at day 1, day 5, day 10, and day 15 after they were intravenously injected with $CuFeSe_2$ NCs (a dose of 20 mg/kg). The blood samples from another four healthy mice without injection of $CuFeSe_2$ NCs were used for comparison. All blood samples were tested to obtain the blood routine and blood chemistry data.

Animal Model. The 4T1 tumor models were generated by subcutaneous injection of 2×10^6 cells in 50 μL of PBS into the flank region of the right back of 5 week old male BALB/c mice (for the MR imaging, CT imaging, SPECT/CT imaging, and PTT treatment) or nude mice (for the PA imaging). Mice were selected for imaging and therapy experiments when their tumors grew to 90 mm^3. All animal experiments were carried out with approval and protocols of the Soochow University Laboratory Animal Center.

Multimodal Imaging Experiments. *Photoacoustic Imaging. In vitro* and *in vivo* PA imaging was performed on a multispectral optoacoustic tomography scanner (MSOT, iThera Medical). A series of $CuFeSe_2$ NC solutions (0, 6, 25, 12.5, 25, 50, and 100 μg/mL) were prepared for *in vitro* testing. To evaluate the imaging performance *in*

DOI: 10.1021/acsnano.7b01032
ACS Nano 2017, 11, 5633−5645

vivo, a nude mouse bearing a tumor was anaesthetized and scanned with MSOT before and after intravenous injection of $CuFeSe_2$ NC solution (0.6 mg/mL, 200 μL).

MRI Measurements. MRI was performed on a clinically used 3.0 T MRI instrument. The longitudinal and transverse relaxivities (*i.e.*, r_1 and r_2) of $CuFeSe_2$ NCs and their *in vitro* T_1- and T_2-weighted MRI images were measured using nanoparticle solutions with different Fe concentrations (0, 0.2, 0.4, 0. 6, 0.8, 1.0 mM of Fe). T_1-weighted MR imaging was performed with a saturation recovery spin−echo sequence (echo time, TE = 7 ms, repetition time, TR = 3000, 2600, 2400, 2200, 2000, 1800, 1600, 1400, 1200, 1100, 1000, 900, 800, 700, 600, 500, 200, and 50 ms). T_2-weighted imaging was conducted with the Carr−Purcell−Meiboom−Gill method using the rapid imaging with refocused echoes (RARE) sequence and the following parameters: TR = 2.0 s, TE = 10−320 ms (time interval is 10 ms). For *in vivo* imaging, the mouse was anesthetized with isoflurane (1.5%) at 1 L/min flow throughout the experiment. $CuFeSe_2$ NCs (200 μL, 2 mg/mL, 20 mg/kg) were administered by intravenous injection. T_1-weighted MRI images were acquired using the T_1-RARE sequence with parameters as follows: TR = 600 ms, TE = 12 ms, field of view = 49 mm × 60 mm, matrix size = 512 × 512, number of slices = 7, slice thickness/gap = 2.0 mm/0.6 mm, flip angle = 160°, and number of excitations, NEX = 2.

CT Imaging. The potential of $CuFeSe_2$ NCs in CT imaging was illustated by comparison with commercial iopromide agent. $CuFeSe_2$ NCs and iopromide solutions with different concentrations (0, 3, 6, 9, 12 mM) were loaded into capsules for measuing Hounsfield units to evaluate their performance. For *in vivo* CT imaging, $CuFeSe_2$ NCs were either intratumorally or intravenously injected into 4T1 tumor-bearing mice, which were placed in an animal bed and anesthetized with isoflurane continuously. The parameters of CT scan are 3 frames averaging, 615 mA tube current, and 55 keV tube voltage.

^{99m}Tc-Labeled $CuFeSe_2$@PTMP−PMAA NCs for SPECT Imaging. First, 2 mCi Na[$^{99m}TcO_4$] (purchased from Shanghai GMS Pharmaceutical Co., Ltd.) was reduced with 200 μL of stannous chloride solution ($SnCl_2$, 1 mg/mL in 0.1 M HCl), and the nanocrystal solution (200 μL, 2 mg/mL) was added into and reacted for 30 min at room temperature. The obtained $CuFeSe_2$−^{99m}Tc NCs were purified by ultrafiltration to remove the free ^{99m}Tc, and the radioactivity of the labeled nanocrystals was determined to be 1.14 mCi. The mice bearing 4T1 tumors were intravenously injected with $CuFeSe_2$−^{99m}Tc NCs for SPECT imaging with an animal SPECT (MILabs, Utrecht, The Netherlands) imaging system at various time points after injection.

Photothermal Therapy. For *in vitro* photothermal ablation of cancer cells, 4T1 cells (8×10^4 cells per well) were seeded into 12-well plates and incubated with $CuFeSe_2$ NCs with concentrations of 0, 50, 100, and 200 μg/mL for 10 h. Then, the cells were irradiated by using an 808 nm laser with 0, 0.75, and 1 W/cm^2 for 5 min and stained with a live/dead kit (Thermo Fisher) for 30 min to distinguish the live cells (green color) and the dead cells (red color) with a fluorescence microscope (OLYMPUS, IX73).

For *in vivo* PTT, $CuFeSe_2$ NCs (200 μL, 2 mg/mL) or PBS solution was intravenously injected into tumor-bearing mice, which were irradiated for 5 min with an 808 nm NIR laser (Hi-Tech Optoelectronics Co., Ltd., Beijing, China) at a power density of 1 W/cm^2. The real-time thermal images of the mice were recorded with an infrared thermal imaging camera (FLIR, A65) during treatment. The tumor size was measured with calipers every 2 days, and the tumor volume (V, mm^3) was calculated as $V = LW^2/2$, where L and W are the length and width of the tumor, respectively.

Blood Circulation Behavior. Blood samples were collected from retinal veins of four healthy BALB/c mice before and after intravenous injection of $CuFeSe_2$ NCs (200 μL, 2 mg/mL) at 0.25, 0.5, 1, 2, 4, 6, 8, 12, 24, 48, and 72 h. The Cu contents in the blood samples were measured by ICP-MS after the samples were digested with a HNO_3/H_2O_2 mixture (ratio of 2:1 HNO_3/H_2O_2 by volume). The decay curve of the Cu contents in the blood was fitted with a two-compartmental model to extract the blood circulation time.

Biodistribution. Eight groups of 4T1 tumor-bearing mice (n = 4 per group) were injected with $CuFeSe_2$ NC solution (200 μL, 2 mg/mL) *via* tail vein. The major organs and tissues, including the heart, liver, spleen, lung, kidney, stomach, intestines, skin, bone, muscle, brain, and tumor, were dissected at 2, 4, 6, 8, 12, 24, 48, and 72 h postinjection, weighed, and digested with the HNO_3/H_2O_2 solution (ratio of 2:1 HNO_3/H_2O_2 by volume). The Cu contents in each organ/tissue were analyzed with ICP-MS.

Histological Analysis. The mice from the control group or treatment groups were sacrificed to resect their heart, liver, spleen, lung, and kidney. These organs were dipped in 10% formalin, embedded in paraffin, cut into a series of slices with 5 μm thickness, and stained with H&E. The histology and morphology of slices were captured with a Leica microscope (DM750).

ASSOCIATED CONTENT

Supporting Information

The Supporting Information is available free of charge on the ACS Publications website at DOI: 10.1021/acsnano.7b01032.

Additional characterization results (TEM, particle size distribution, EELS, XPS, XRD, UV−vis−NIR absorption, FTIR, TGA, DLS) of $CuFeSe_2$ NCs, determination and calculation of photothermal conversion efficiency, colloidal stability and radiostability, biodistribution of ^{99m}Tc-$CuFeSe_2$ NCs, signal intensities in tumor from SPCET/CT images, PA images and MRI images, PA images of liver and spleen, photothermal ablation of tumor cells or tumor, photographs of mice, slices of major organs stained with H&E (PDF)

AUTHOR INFORMATION

Corresponding Author

*E-mail: zhenli@suda.edu.cn.

ORCID

Mingyuan Gao: 0000-0002-7360-3684

Zhen Li: 0000-0003-0333-7699

Notes

The authors declare no competing financial interest.

ACKNOWLEDGMENTS

Z.L. acknowledges support from the National Natural Science Foundation of China (81471657, 81527901), the 1000 Plan for Young Talents, and Jiangsu Specially Appointed Professorship. The authors also are grateful for support from the Jiangsu Provincial Key Laboratory of Radiation Medicine and Protection, the Priority Academic Development Program of Jiangsu Higher Education Institutions (PAPD). The authors also thank Dr. Tania Silver for helpful discussion.

REFERENCES

(1) Cheng, L.; Wang, C.; Feng, L.; Yang, K.; Liu, Z. Functional Nanomaterials for Phototherapies of Cancer. *Chem. Rev.* **2014**, *114*, 10869−10939.

(2) Jaque, D.; Martinez Maestro, L.; del Rosal, B.; Haro-Gonzalez, P.; Benayas, A.; Plaza, J. L.; Martin Rodriguez, E.; Garcia Sole, J. Nanoparticles for Photothermal Therapies. *Nanoscale* **2014**, *6*, 9494−9530.

(3) Sun, C.; Wen, L.; Zeng, J.; Wang, Y.; Sun, Q.; Deng, L.; Zhao, C.; Li, Z. One-Pot Solventless Preparation of Pegylated Black Phosphorus Nanoparticles for Photoacoustic Imaging and Photothermal Therapy of Cancer. *Biomaterials* **2016**, *91*, 81−89.

(4) Chen, M.; Tang, S.; Guo, Z.; Wang, X.; Mo, S.; Huang, X.; Liu, G.; Zheng, N. Core-Shell Pd@Au Nanoplates as Theranostic Agents

for *in-Vivo* Photoacoustic Imaging, CT Imaging, and Photothermal Therapy. *Adv. Mater.* **2014**, *26*, 8210−8216.
(5) Cui, J.; Jiang, R.; Xu, S.; Hu, G.; Wang, L. Cu_7S_4 Nanosuperlattices with Greatly Enhanced Photothermal Efficiency. *Small* **2015**, *11*, 4183−4190.
(6) Wen, L.; Chen, L.; Zheng, S. M.; Zeng, J. F.; Duan, G. X.; Wang, Y.; Wang, G. L.; Chai, Z. F.; Li, Z.; Gao, M. Y. Ultrasmall Biocompatible WO_{3-x} Nanodots for Multi-Modality Imaging and Combined Therapy of Cancers. *Adv. Mater.* **2016**, *28*, 5072−5079.
(7) Zeng, J.; Cheng, M.; Wang, Y.; Wen, L.; Chen, L.; Li, Z.; Wu, Y.; Gao, M.; Chai, Z. Ph-Responsive Fe(III)-Gallic Acid Nanoparticles for *in Vivo* Photoacoustic-Imaging-Guided Photothermal Therapy. *Adv. Healthcare Mater.* **2016**, *5*, 772−780.
(8) Zheng, X.; Xing, D.; Zhou, F.; Wu, B.; Chen, W. R. Indocyanine Green-Containing Nanostructure as near Infrared Dual-Functional Targeting Probes for Optical Imaging and Photothermal Therapy. *Mol. Pharmaceutics* **2011**, *8*, 447−456.
(9) Li, B.; Wang, Q.; Zou, R.; Liu, X.; Xu, K.; Li, W.; Hu, J. $Cu_{7.2}S_4$ Nanocrystals: A Novel Photothermal Agent with a 56.7% Photothermal Conversion Efficiency for Photothermal Therapy of Cancer Cells. *Nanoscale* **2014**, *6*, 3274−3282.
(10) Zhang, S.; Sun, C.; Zeng, J.; Sun, Q.; Wang, G.; Wang, Y.; Wu, Y.; Dou, S.; Gao, M.; Li, Z. Ambient Aqueous Synthesis of Ultrasmall Pegylated $Cu_{2-x}Se$ Nanoparticles as a Multifunctional Theranostic Agent for Multimodal Imaging Guided Photothermal Therapy of Cancer. *Adv. Mater.* **2016**, *28*, 8927−8936.
(11) Li, B.; Yuan, F.; He, G.; Han, X.; Wang, X.; Qin, J.; Guo, Z. X.; Lu, X.; Wang, Q.; Parkin, I. P.; Wu, C. Ultrasmall $CuCo_2S_4$ Nanocrystals: All-in-One Theragnosis Nanoplatform with Magnetic Resonance/near-Infrared Imaging for Efficiently Photothermal Therapy of Tumors. *Adv. Funct. Mater.* **2017**, *27*, 1606218.
(12) Xiao, J. W.; Fan, S. X.; Wang, F.; Sun, L. D.; Zheng, X. Y.; Yan, C. H. Porous Pd Nanoparticles with High Photothermal Conversion Efficiency for Efficient Ablation of Cancer Cells. *Nanoscale* **2014**, *6*, 4345−4351.
(13) Prodi, L.; Rampazzo, E.; Rastrelli, F.; Speghini, A.; Zaccheroni, N. Imaging Agents Based on Lanthanide Doped Nanoparticles. *Chem. Soc. Rev.* **2015**, *44*, 4922−4952.
(14) Ghosh, S.; Avellini, T.; Petrelli, A.; Kriegel, I.; Gaspari, R.; Almeida, G.; Bertoni, G.; Cavalli, A.; Scotognella, F.; Pellegrino, T.; Manna, L. Colloidal $CuFeSe_2$ Nanocrystals: Intermediate Fe d-Band Leads to High Photothermal Conversion Efficiency. *Chem. Mater.* **2016**, *28*, 4848−4858.
(15) Zhao, Q.; Yi, X.; Li, M.; Zhong, X.; Shi, Q.; Yang, K. High Near-Infrared Absorbing Cu_5FeS_4 Nanoparticles for Dual-Modal Imaging and Photothermal Therapy. *Nanoscale* **2016**, *8*, 13368−13376.
(16) Hamdadou, N.; Morsli, M.; Khelil, A.; Bernède, J. C. Fabrication of N- and P-Type Doped $CuFeSe_2$ Thin Films Achieved by Selenization of Metal Precursors. *J. Phys. D: Appl. Phys.* **2006**, *39*, 1042−1049.
(17) Bernede, J. C.; Hamdadou, N.; Khelil, A. X-Ray Photoelectron Spectroscopy Study of $CuFeSe_2$Thin Films. *J. Electron Spectrosc. Relat. Phenom.* **2004**, *141*, 61−66.
(18) Hsu, Y. K.; Lin, Y. G.; Chen, Y. C. One-Pot Synthesis of $CuFeSe_2$ Cuboid Nanoparticles. *Mater. Res. Bull.* **2011**, *46*, 2117−2119.
(19) Kradinova, L. V.; Polubotko, A. M.; Popov, V. V.; Prochukhan, V. D.; Rud, Yu. V.; Skoriukin, V. E. Novel Zero-Gap Compounds, Magnetics: $CuFeSe_2$ and $CuFeTe_2$. *Semicond. Sci. Technol.* **1993**, *8*, 1616.
(20) Wang, W.; Jiang, J.; Ding, T.; Wang, C.; Zuo, J.; Yang, Q. Alternative Synthesis of $CuFeSe_2$ Nanocrystals with Magnetic and Photoelectric Properties. *ACS Appl. Mater. Interfaces* **2015**, *7*, 2235−2241.
(21) Lu, Q.; Hu, J.; Tang, K.; Deng, B.; Qian, Y.; Li, Y. The Synthesis of $CuFeSe_2$ through a Solventothermal Process. *J. Cryst. Growth* **2000**, *217*, 271−273.
(22) Longmire, M.; Choyke, P. L.; Kobayashi, H. Clearance Properties of Nano-Sized Particles and Molecules as Imaging Agents: Considerations and Caveats. *Nanomedicine* **2008**, *3*, 703−717.
(23) Liu, J.; Yu, M.; Zhou, C.; Zheng, J. Renal Clearable Inorganic Nanoparticles: A New Frontier of Bionanotechnology. *Mater. Today* **2013**, *16*, 477−486.
(24) Han, C.; Li, Z.; Lu, G. Q.; Xue Dou, S. Robust Scalable Synthesis of Surfactant-Free Thermoelectric Metal Chalcogenide Nanostructures. *Nano Energy* **2015**, *15*, 193−204.
(25) Han, C.; Sun, Q.; Cheng, Z. X.; Wang, J. L.; Li, Z.; Lu, G. Q.; Dou, S. X. Ambient Scalable Synthesis of Surfactant-Free Thermoelectric Cuagse Nanoparticles with Reversible Metallic-N-P Conductivity Transition. *J. Am. Chem. Soc.* **2014**, *136*, 17626−17633.
(26) Wang, Z.; Tan, B.; Hussain, I.; Schaeffer, N.; Wyatt, M. F.; Brust, M.; Cooper, A. I. Design of Polymeric Stabilizers for Size-Controlled Synthesis of Monodisperse Gold Nanoparticles in Water. *Langmuir* **2007**, *23*, 885−895.
(27) Hussain, I.; Graham, S.; Wang, Z.; Tan, B.; Sherrington, D. C.; Rannard, S. P.; Cooper, A. I.; Brust, M. Size-Controlled Synthesis of near-Monodisperse Gold Nanoparticles in the 1−4 nm Range Using Polymeric Stabilizers. *J. Am. Chem. Soc.* **2005**, *127*, 16398−16399.
(28) Nakamoto, K. Infrared and Raman Spectra of Inorganic and Coordination Chemistry. *Part A: Theory and Applications in Inorganic Chemistry*, 5th edn.; Wiley: New York, 1977.
(29) Sun, Z.; Xie, H.; Tang, S.; Yu, X.-F.; Guo, Z.; Shao, J.; Zhang, H.; Huang, H.; Wang, H.; Chu, P. K. Ultrasmall Black Phosphorus Quantum Dots: Synthesis and Use as Photothermal Agents. *Angew. Chem., Int. Ed.* **2015**, *54*, 11526−11530.
(30) Woolley, J. C.; Lamarche, A. M.; Lamarche, G.; Quintero, M.; Swainson, I. P.; Holden, T. M. Low Temperature Magnetic Behaviour of $CuFeSe_2$ from Neutron Diffraction Data. *J. Magn. Magn. Mater.* **1996**, *162*, 347−354.
(31) Polubotko, A. M. Ferron-Type Conductivity in Metallic $CuFeSe_2$. *Phys. Met. Metallogr.* **2011**, *112*, 589−590.
(32) Lamazares, J.; Jaimes, E.; D'Onofrio, L.; Gonzalez-Jimenez, F.; Sanchez Porras, G.; Tovar, R.; Quintero, M.; Gonzalez, J.; Woolley, J. C.; Lamarche, G. Magnetic Susceptibility, Transport and Mössbauer Measurements in $CuFeSe_2$. *Hyperfine Interact.* **1991**, *67*, 517−521.
(33) Wang, Y.; Jiang, C.; He, W.; Ai, K.; Ren, X.; Liu, L.; Zhang, M.; Lu, L. Targeted Imaging of Damaged Bone *in Vivo* with Gemstone Spectral Computed Tomography. *ACS Nano* **2016**, *10*, 4164−4172.
(34) Lee, N.; Choi, S. H.; Hyeon, T. Nano-Sized CT Contrast Agents. *Adv. Mater.* **2013**, *25*, 2641−2660.
(35) Seltzer, S. M. Calculation of Photon Mass Energy-Transfer and Mass Energy-Absorption Coefficients. *Radiat. Res.* **1993**, *136*, 147−170.
(36) Mao, F.; Wen, L.; Sun, C.; Zhang, S.; Wang, G.; Zeng, J.; Wang, Y.; Ma, J.; Gao, M.; Li, Z. Ultrasmall Biocompatible Bi_2Se_3 Nanodots for Multimodal Imaging-Guided Synergistic Radiophotothermal Therapy against Cancer. *ACS Nano* **2016**, *10*, 11145−11155.
(37) Na, H. B.; Lee, J. H.; An, K.; Park, Y. I.; Park, M.; Lee, I. S.; Nam, D.-H.; Kim, S. T.; Kim, S.-H.; Kim, S.-W.; Lim, K.-H.; Kim, K.-S.; Kim, S.-O.; Hyeon, T. Development of a T_1 Contrast Agent for Magnetic Resonance Imaging Using Mno Nanoparticles. *Angew. Chem.* **2007**, *119*, 5493−5497.
(38) Nam, J.; Won, N.; Bang, J.; Jin, H.; Park, J.; Jung, S.; Jung, S.; Park, Y.; Kim, S. Surface Engineering of Inorganic Nanoparticles for Imaging and Therapy. *Adv. Drug Delivery Rev.* **2013**, *65*, 622−648.
(39) Ye, L.; Yong, K.-T.; Liu, L.; Roy, I.; Hu, R.; Zhu, J.; Cai, H.; Law, W.-C.; Liu, J.; Wang, K.; Liu, J.; Liu, Y.; Hu, Y.; Zhang, X.; Swihart, M. T.; Prasad, P. N. A Pilot Study in Non-Human Primates Shows No Adverse Response to Intravenous Injection of Quantum Dots. *Nat. Nanotechnol.* **2012**, *7*, 453−458.
(40) Li, Z.; Tan, B.; Allix, M.; Cooper, A. I.; Rosseinsky, M. J. Direct Coprecipitation Route to Monodisperse Dual-Functionalized Magnetic Iron Oxide Nanocrystals without Size Selection. *Small* **2008**, *4*, 231−239.
(41) Li, Z.; Yi, P. W.; Sun, Q.; Lei, H.; Zhao, H. L.; Zhu, Z. H.; Smith, S. C.; Lan, M. B.; Lu, G. Q. M. Ultrasmall Water-Soluble and

DOI: 10.1021/acsnano.7b01032
ACS Nano 2017, 11, 5633−5645

Biocompatible Magnetic Iron Oxide Nanoparticles as Positive and Negative Dual Contrast Agents. *Adv. Funct. Mater.* **2012**, *22*, 2387–2393.

(42) Li, Z.; Wang, S. X.; Sun, Q.; Zhao, H. L.; Lei, H.; Lan, M. B.; Cheng, Z. X.; Wang, X. L.; Dou, S. X.; Max Lu, G. Q. Ultrasmall Manganese Ferrite Nanoparticles as Positive Contrast Agent for Magnetic Resonance Imaging. *Adv. Healthcare Mater.* **2013**, *2*, 958–964.

DOI: 10.1021/acsnano.7b01032
ACS Nano 2017, 11, 5633–5645